Flow field and performance analysis of an integrated diverterless supersonic inlet

J. Masud
Jehanzeb.Masud@mail.au.edu.pk
Department of Mechanical & Aerospace Engineering
Institute of Avionics & Aeronautics
Air University, Islamabad
Pakistan

ABSTRACT

In this paper the computed flow and performance characteristics at low angle-of-attack (AOA) of an integrated diverterless supersonic inlet (DSI) are presented. The subsonic characteristics are evaluated at M_∞ = 0·8 while the supersonic characteristics are evaluated at M_∞ = 1·7, which is near the design Mach number for the intake. In addition to the external flow features, the internal intake duct flow behaviour is also evaluated. The results of this study indicate effective boundary layer diversion due to the 'bump' compression surface in both subsonic and supersonic regimes. At M_∞ = 1·7, the shockwave structure (oblique/normal shockwave) on the 'bump' compression surface and intake inlet is satisfactory at design (critical) mass flow rate. The intake duct flow behaviour at subsonic and supersonic conditions is generally consistent with 'Y' shaped intake duct of the present configuration. The secondary flow structure inside the duct has been effectively captured by present computations. The computed intake total pressure recovery at M_∞ = 1·7 exhibits higher-than-conventional behaviour at low mass flow ratios, which is attributed to unique inlet design. Overall computed subsonic and supersonic total pressure recovery characteristics are satisfactory under the evaluated conditions and are also in agreement with wind tunnel test data.

NOMENCLATURE

AOA	angle-of-attack
Ac	intake capture area
m	intake mass flow ratio
β	side slip angle
CFD	computational fluid dynamics
Cp	pressure coefficient $(P–P_\infty)/½\rho_\infty V_\infty^2$
DSI	diverterless supersonic inlet
M	Mach number
M_∞	Free stream Mach number
P	static pressure
P_o	total pressure
P_∞	free stream static pressure
SA	one equation Spalarat-Allamaras turbulence model
σ	intake total pressure ratio
V_∞	free stream velocity
ρ_∞	free stream density
WTT	wind-tunnel test
x, y, z	Cartesian ordinates
y^+	non-dimensional length scale associated with turbulence model

Paper No. 3556. Manuscript received 16 March 2010, revised 25 January 2011, accepted 8 April 2011.

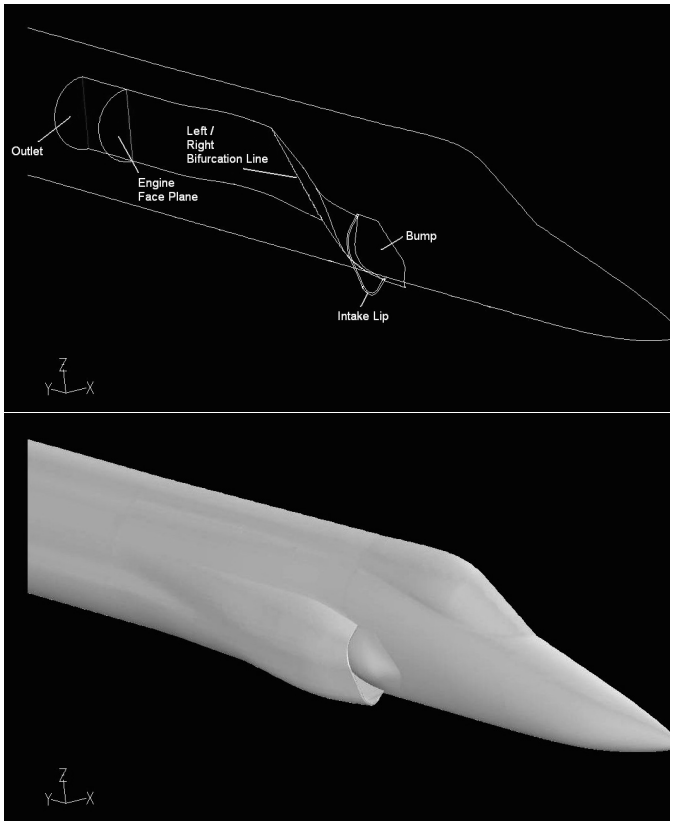

Figure 1. Geometric layout of the intake and the forward fuselage.

1.0 INTRODUCTION

Diverterless supersonic inlet (DSI), also referred to as the bump inlet, has been the focus of renewed research after initial NASA work in the 1950s[1]. This renewed focus stems from its lack of a boundary layer diverter that makes it stealthier compared to other conventional inlets[2]. Researchers have also found certain favourable characteristics of DSI compared to other 'fixed' inlets[3-6], such as higher total pressure recovery, lower flow distortion, better compatibility at supersonic speeds, etc. that make it suitable for application on supersonic aircraft[7-10].

The design of the contoured bump and the intake cowl is primarily based on conical shockwave concept[3,4,14,25,26] that has to be adjusted for forward fuselage (upstream) effects such as modified pressure and Mach number distribution. The bump compression surface contour is based on deflection experienced by a series of flow particles that pass through the 3D shockwave generated by a virtual right circular cone (or other variations thereof) placed in uniform supersonic flow. These flow particles are released at some distance away from cone apex and their trajectory is computationally tracked. The locus of the trajectory of these flow particles defines the initial contour of the bump compression surface. The inlet cowl location and shape is also governed by the initial shockwave generated by the virtual cone. The inlet cowl design typically has a forward sweep, which in combination of the bump compression surface helps to divert the boundary layer away from the intake at all Mach numbers. The choice of virtual cone, the free stream Mach number, the location of release of flow particles, the location of intake cowl etc. are based on individual design needs and specifications. The detailed DSI design concepts are available in Lockheed Martin patents[25,26].

The past work on DSI includes experimental and computational studies on model configurations[4-7,10,23] to investigate various flow features. The application of top-mounted DSI on an unmanned ariel vehicle has been studied by Tan *et al*[20,21] who reported favourable

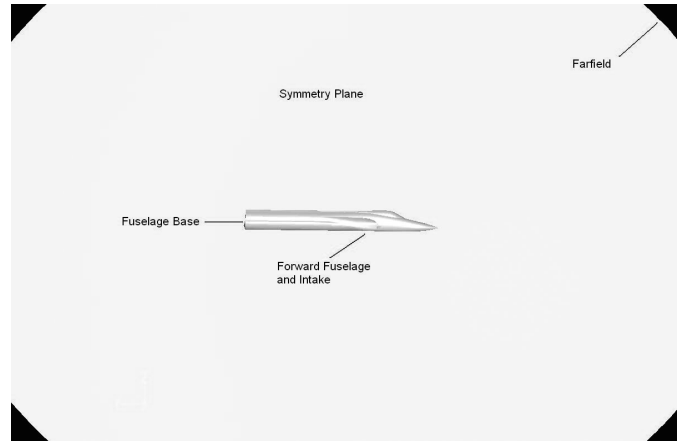

Figure 2. Layout of the computational domain.

flow characteristics over the investigated flight regime. The ventral DSI experimental investigation on a model configuration has been reported by Xie[6,7] with detailed pressure and flow distortion results that indicate maximum pressure recovery around $M_\infty = 1$ that is generally insensitive to moderate variation in angle of attack and side slip angle. The recent experimental and numerical work of Li *et al*[3] on side mounted DSI with forward fuselage on a realistic trainer aircraft configuration has showed generally higher computed total pressure recovery (0·02 ~ 0·04) compared to experimental results. In their work[3] they have also computed the characteristics of an equivalent splitter plate/wedge inlet and have shown improved performance of the DSI. Practical implementation of this work[3] on the realistic trainer aircraft has not been reported in literature.

Presently there are two under-development aircraft that have successfully integrated DSI, one is F-35 Joint Strike Fighter[11] and the other is China and Pakistan co-developed multi-role fighter aircraft[12-14]. As with all supersonic aircraft, airframe, intake and engine integration is a challenging task and DSI is no exception. The basic DSI design features (without specific details) of the two successfully integrated DSIs are available in the works of Hamstra *et al*[25,26], Wooden[11] and Yang[14]. The work of Yang[14] is generally experimental in nature with some basic supersonic computed flow field cases, however flow field details and off-design analysis are not part of the report.

The present paper is based on computational analysis of an integrated DSI[12,14]. In this study the focus is on basic flow and performance characteristic at zero angle-of-attack (AOA) and zero side-slip angle (b). The analysis at higher (non-zero) AOA and β are planned as a later study on DSI. In the present work CFD analysis is carried out at subsonic and supersonic Mach numbers with basic validation of computed results done by wind tunnel test (WTT) data[14], which is available as part of aircraft development process. Typically, in inlet integration testing and analysis, only the forward fuselage and the intake are modelled as shown in Fig. 1, therefore same strategy has been adopted in the present CFD study.

2.0 COMPUTATIONAL SETUP

For the present 3D CFD analysis, right half of forward fuselage and intake are modelled with a plane of symmetry. The co-ordinate system and other parameters of the inlet/forward fuselage are shown in Figs 1 and 2. The intake outlet has been modelled about one intake-diameter away from the engine face so as to avoid the effect of applied boundary conditions on flow characteristics at engine face (Fig. 1). For CFD analysis, in addition to the fuselage/intake combination, the complete flow domain is modelled that includes the free stream far field and the symmetry plane. The far field is kept about

https://doi.org/10.1017/S0001924000006114 Published online by Cambridge University Press

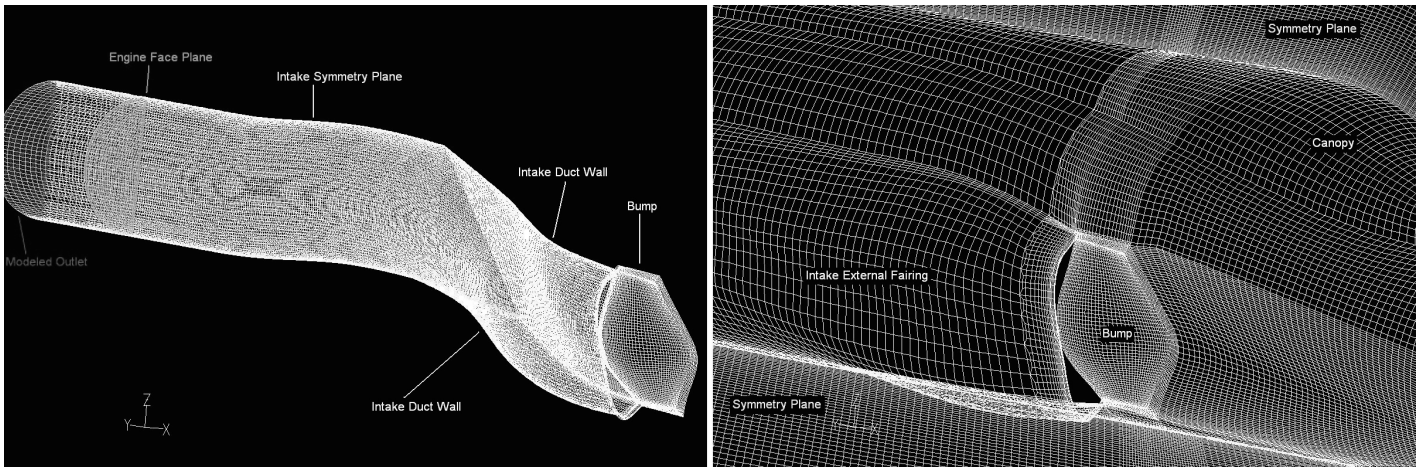

Figure 3. Surface mesh strategy for the intake, fuselage and symmetry plane.

20 times the fuselage maximum diameter away to model free flight conditions and to avoid the far field pressure boundary to influence the pressure distribution in the vicinity of the intake/fuselage. A hypothetical blunt fuselage base was modelled (Fig. 2) on which free stream (far field) flow properties were enforced, which resulted in no blunt body wake or excessive flow gradients that would compromise the quality of computations.

Structured meshing strategy was used for the fuselage and intake surfaces as shown in Fig. 3. Nodes/cells were concentrated towards the surface of fuselage and the intake walls in order to accurately resolve the flow phenomena in their vicinity. Mesh was also concentrated in the bump and intake duct region for the same purpose (Fig. 3). The structured surface mesh was extended into the domain volume by a 'Cooper' meshing strategy[15]. The 'Cooper' meshing scheme[15] uses the surface mesh on a single face of a hexahedral volume and projects it on the corresponding opposite face in a controlled (specified) step-by-step manner in the projection direction, which results in a corresponding volume mesh. The fuselage mesh was progressively made coarser downstream of the intake inlet as this area (intake external fairing, Fig. 3) has little effect in intake characteristics but contributes to computational cost. A representative surface mesh for the present study is shown in Fig. 3.

In the present work, compressible Reynolds Averaged Navier-Stokes (RANS) system of equations with ideal gas model of air was solved using the density based formulation with explicit algorithm of Fluent® CFD code[15-17]. For flow, second order upwind scheme was selected with appropriate values of under relaxation parameters. For computations with the explicit algorithm, four-level multi-grid was employed. The problem was partitioned into four regions for parallel computing.

For boundary conditions, no-slip velocity condition was enforced at the surfaces/walls of fuselage and intake (Figs 1, 2 and 3). Pressure/velocity boundary conditions were used at far field and fuselage base corresponding to the desired free stream Mach number and angle-of-attack. Pressure boundary condition was applied at intake duct outlet (Fig. 3) to control the intake mass flow rate. Symmetry boundary condition was specified on the symmetry planes of the fuselage external domain and the intake internal domain (Fig. 3)[17].

2.1 Turbulence model

For the present study, the one-equation Spalart-Allmaras (SA)[17,18] turbulence model is used due to its demonstrated feasibility for Aerospace applications, such as the present configuration. Although Spalart-Allmaras is a low Reynolds number model, however for the wall treatment, standard wall functions formulation of Fluent for SA model was used[17]. This reduces the computational cost by allowing somewhat coarser mesh near solid walls based on y^+. The integrated results (total pressure on engine face, etc.) of the present analysis are generally consistent with the experimental data[14] (to be discussed later in this paper), therefore further trials with different turbulence models was not done.

2.2 Grid density

Numerically computed results may change with the type and fineness of the mesh/grid used for computations. For the present study the mesh used has 2·71 million cells with 2·78 million nodes (Fig. 3). For the present grid, the value of computed turbulent law y^+ remains below 100 and 200 at subsonic and supersonic speeds[17] in the regions of intake duct, bump compression surface and the forward fuselage upstream of the bump compression surface. These values of turbulent law y^+ show reasonable resolution of grid near the walls with respect to the usage of standard wall functions[17]. The comparison of integrated quantities at engine inlet face with the experimental data[14] is quite reasonable (to be discussed later in this paper), therefore the mesh with 2·8m nodes is considered adequate for the present study.

3.0 RESULTS AND DISCUSSION

In the present study, computations were carried out at Mach numbers of 0·8 and 1·7 in order to see the subsonic and supersonic performance of DSI. The angle-of-attack was set to zero for the present computations. Side-slip angle is inherently zero for the present study due to the use of symmetry planes (Figs 2 and 3, right half fuselage and intake modelled). In an intake analysis the results are dependent on intake mass flow rate, which is expressed in terms of intake mass flow ratio 'm' i.e., the ratio of intake mass flow to that of hypothetical free stream mass flow through the intake capture area. Generally, the subsonic (M = 0·8) results presented here correspond to an intake mass flow ratio 'm' of around ~0·7 while the supersonic (M = 1·7) results correspond to 'm' around ~0·8. However, the intake performance at M = 0·8 and M = 1·7 presented later in this paper includes results for a series of intake mass flow ratios. The intake total pressure ratio/recovery used in the present study, as in intake analysis literature, is the ratio of average total pressure on engine face plane to the free stream total pressure.

3.1 Subsonic flow field in vicinity of fuselage/intake combination

The subsonic flow field around the forward fuselage and the intake consists of free stream flow being modified by the presence of these bodies. The flow adjacent to the fuselage/intake generally follows

https://doi.org/10.1017/S0001924000006114 Published online by Cambridge University Press

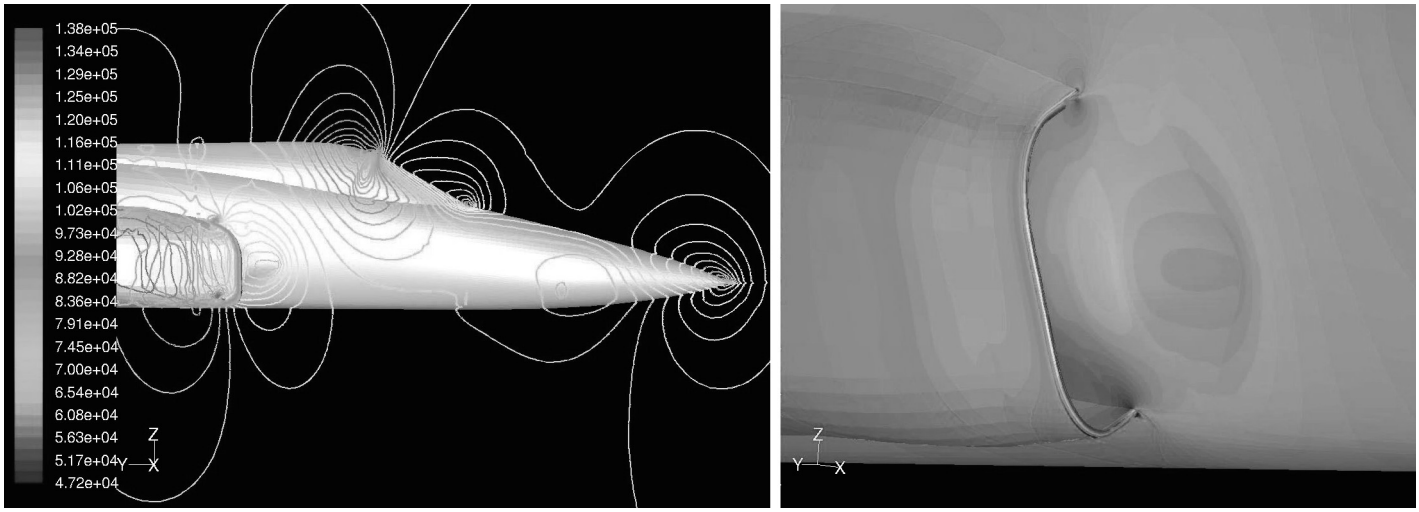

Figure 4. Pressure (Pa) distribution at M_∞= 0·8 on forward fuselage and symmetry plane (left) and in the vicinity of the bump compression surface (right).

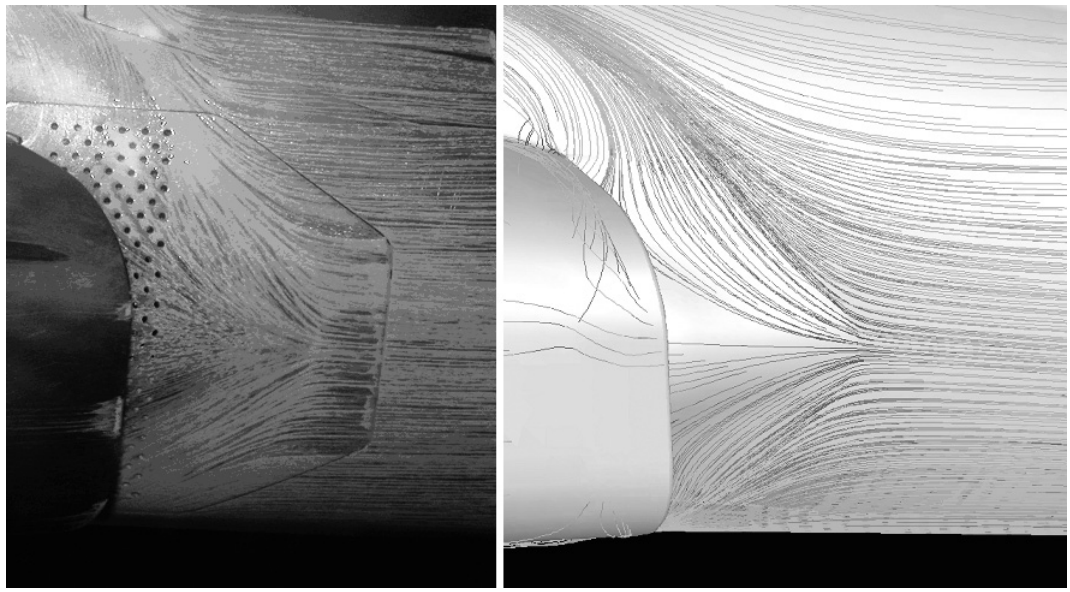

Figure 5. Experimental (left)[14] and computed flow traces at subsonic speed.

their contour while far away it merges with the free stream flow. Figure 4 shows the pressure variation on the fuselage surface, symmetry plane as well as in the vicinity of the bump compression surface for M = 0·8 (AOA = 0°). This figure is generally representative of flow field at all subsonic Mach numbers at relatively high mass flow ratios. The subsonic flow adjustment (slowing down) ahead of the fuselage, canopy and the bump compression surface of the intake are evident from Fig. 4. The velocity vector plot (not shown here for brevity) shows attached flow on the fuselage and in the vicinity of the intake. The pressure field in the vicinity of the bump compression surface shows positive pressure gradients away from the bump, which effectively diverts the upstream boundary layer away from the inlet. This phenomenon is discussed next with the help of surface flow traces.

The computed surface flow traces in the vicinity of the intake inlet is shown in Fig. 5. Certain spurious flow traces are visible due to graphics rendering limitation of the software in completely eliminating hidden features. The wind-tunnel test oil flow traces[14] under low angle-of-attack subsonic conditions are also included for comparison. The upstream boundary layer diversion due the bump compression surface is evident. This is consistent with the surface pressure distribution shown in Fig. 4. The qualitative agreement between computed and wind-tunnel test flow traces is apparent.

3.2 Supersonic flow field in vicinity of fuselage/intake combination

The supersonic flow field around the forward fuselage and intake consists of free stream flow being modified by shock and expansion waves due to the presence of these bodies. Figure 6 shows the pressure variation on the fuselage surface, symmetry plane as well as in the vicinity of the bump compression surface for M = 1·7 (AOA = 0°). These figures are generally representative of flow field at all supersonic Mach numbers at relatively large intake mass flow ratio. The supersonic flow adjustment around forward fuselage and the intake is characterised by three dimensional shock and expansion waves as evident from Fig. 6. On bump compression surface the 'W' shaped imprint of a strong terminal (normal) shock wave is apparent, this is consistent with an earlier design study[14]. The pressure distribution behind this 'W' shaped imprint of the terminal shock wave on

https://doi.org/10.1017/S0001924000006114 Published online by Cambridge University Press

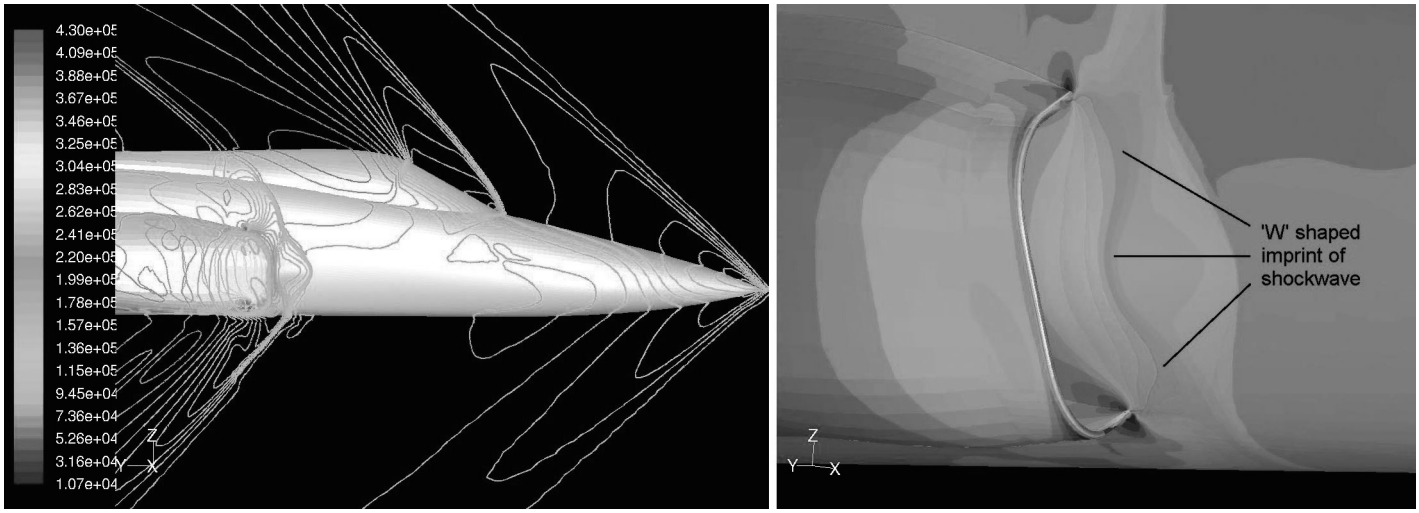

Figure 6. Pressure (Pa) distribution at M_∞ = 1·7 on forward fuselage and symmetry plane (left) and in the vicinity of the bump compression surface (right).

the bump surface shows outward positive pressure gradients, which effectively diverts the upstream boundary layer away from the inlet from behind the terminal (normal) shock wave. This aspect is discussed later in the paper with the help of flow traces figure. The inlet cowl of this DSI is designed with a forward sweep that facilitates the diversion of the boundary layer[14] as well.

The detailed shock wave structure in the vicinity of the bump compression surface and the inlet cowl is shown in Fig. 7. Mach number distribution on seven equally spaced horizontal planes is shown for this purpose. Oblique shock waves originate from the leading edges of the bump compression surface as seen from this figure (Fig. 7). Normal shock wave is apparent just short of the inlet. The imprint of this normal shock wave on the bump surface forms the 'W' shape (Fig. 6), as discussed earlier. The oblique shock and normal shock wave impinge near the cowl lip, which shows a relatively high intake mass flow ratio near intake design point.

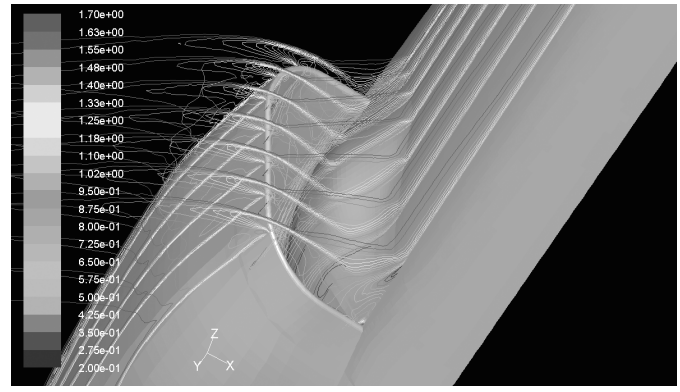

Figure 7. Mach number distribution on seven horizontal planes (parallel to *x-y* plane) in the vicinity of the intake inlet at M_∞ = 1·7.

3.3 Flow field inside the intake duct

The external flow field of a fuselage/intake combination is important since it determines not only the quality of air available to the engine but also the intake drag of the aircraft. This becomes even more important for a supersonic aircraft. The internal flow field of an intake duct plays an equally important role in determining the quality of air (total pressure, Mach number and flow distortion) to the engine. The computed intake duct surface pressure distribution at M = 0·8 and M = 1·7 is shown in Fig. 8. This figure is an extension of the pressure distributions shown in Fig. 4 and 6 for M = 0·8 and M = 1·7, respectively. Progressive pressure increase in the duct towards engine face plane, for both subsonic and supersonic free stream conditions, is evident and is consistent with subsonic flow in slightly diverging (increasing cross-section area) intake duct of the present study. The areas of relatively higher local static pressure at compression-type-turning of the flow in concave regions of intake duct are evident. Similarly, areas of relatively lower local static pressure at expansion-type-turning of the flow in convex regions of intake duct are also evident from Fig. 8.

The traces of 3D flow inside the intake duct are shown in Fig. 9 for M = 0·8 and M = 1·7. The swirling secondary flow due to the Y-shaped intake duct (S-shaped due to symmetry) is evident and is primarily caused by the overall duct curvature. The difference in swirl for subsonic and supersonic free stream is evident. Apparently the combination of boundary layer diversion, inlet shock structure and shockwave-boundary layer interaction causes greater duct flow swirl at supersonic Mach numbers. At M = 1·7 the low energy boundary layer is forced out of the intake from behind the normal shock (Figs 6 and 7) as discussed earlier. This spilled out air from the top and bottom portion of the inlet is evident from Fig. 9. The spilled out air from the top and bottom portion of the inlet interacts with the external flow and causes shock waves as seen from the pressure distribution on the fuselage surface and symmetry plane in Fig. 6.

The nature of swirl, or secondary flow, induced by the Y-shaped intake duct and upstream flow on the engine face plane is shown in Fig. 10 by plotting the in-plane uniform-length velocity vectors that have been colored by the local total pressure. Stronger secondary flow that occupies larger region of engine face plane is evident at M = 1·7 compared to M = 0·8. The development of this secondary flow along with other flow features inside the intake duct have been discussed earlier in this paper.

The total pressure distribution on the engine face plane at M = 0·8 and M = 1·7 is shown in Fig. 11. At M = 0·8 there is a larger region on engine face plane with total pressure near the free stream total pressure value compared to M = 1·7. This indicates higher total pressure recovery at M = 0.8 compared to M = 1.7, which is typical of supersonic external compression intakes, such as the present DSI. The region of relatively lower total pressure distribution at M = 0.8 (Fig. 11) also corresponds to region of stronger secondary flow (Fig. 10, M = 0·8) as well as the wake generated by the intake left-right bifurcation wall (Figs 1 and 3). Similarly, the region of relatively

https://doi.org/10.1017/S0001924000006114 Published online by Cambridge University Press

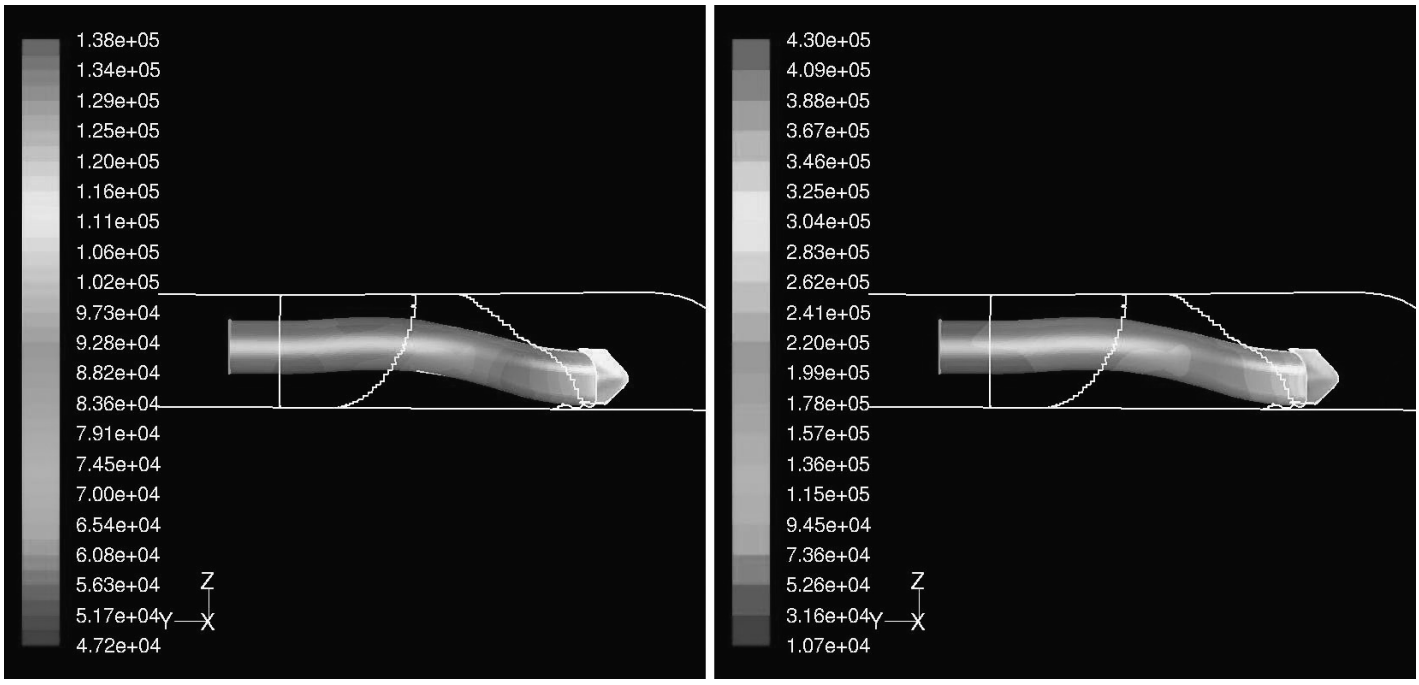

Figure 8. Overall surface pressure (Pa) distribution on the intake duct at M_∞ = 0·8 (left) and M_∞ = 1.7 (right).

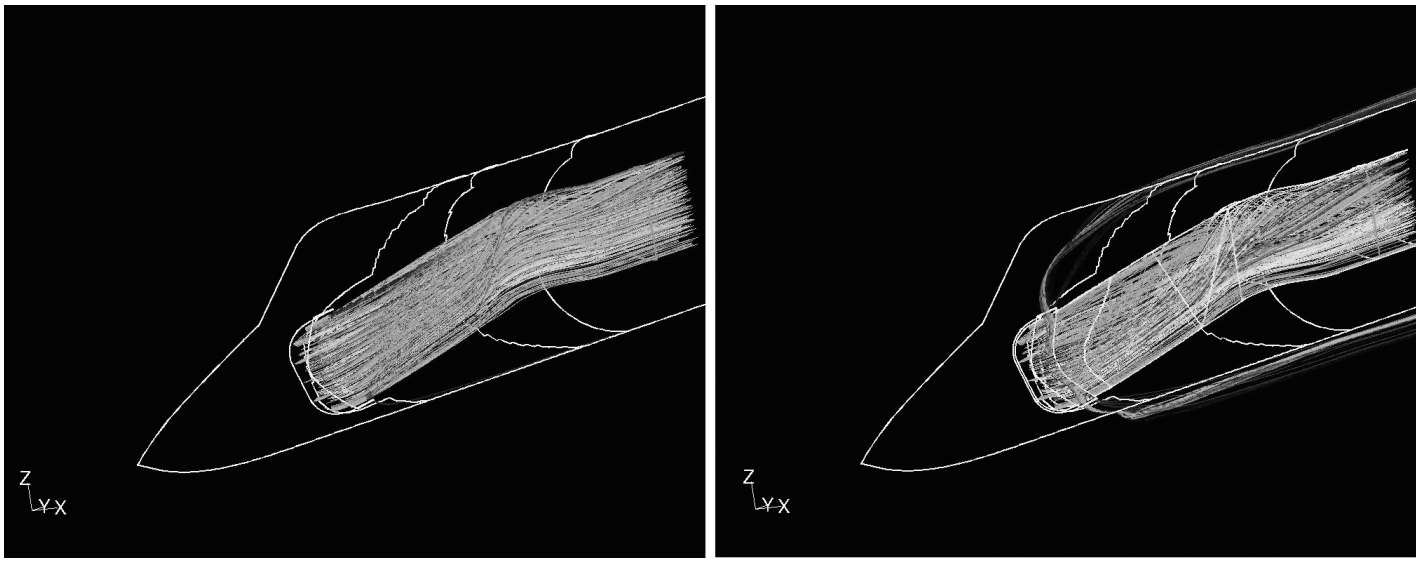

Figure 9. Stream traces of flow in the intake duct at M_∞ = 0·8 (left) and M_∞ = 1·7 (right).

lower total pressure distribution at M = 1·7 (Fig. 11) also corresponds to region of stronger secondary flow (Fig. 10, M = 1·7) as well. At M = 1·7, the presence of external shock waves (Figs 6 and 7) cause additional loss of total pressure, therefore the over all total pressure recovery at engine face plane is lower than M = 0·8, which is typical of external compression fixed intakes.

3.4 Performance characteristics of DSI

The performance of an intake system is quantified by the total pressure recovery and flow distortion at the engine face for a range of free stream conditions (M, AOA, β, etc.). The DSI pressure recovery characteristics at engine face plane (Figs 1 and 3) at free stream conditions of M = 0·8 and M = 1·7 at AOA = 0° and β = 0°, for a range of intake mass flow ratios, is presented in Figs 12 and 13, respectively. An experimental data point from a wind tunnel test[14] is also included for comparison. Reasonable agreement between computed and experimental data at a particular intake mass flow ratio is apparent. At subsonic speeds (Fig. 12), the reduction in total pressure recovery with increasing intake mass flow ratio is consistent with increased viscous/turbulent losses associated with increased flow velocity in the intake. Intake lip flow separation also contributes to increased viscous losses at relatively higher mass flow ratios, typically beyond the intake design mass flow rate[19]. The intake chocking is indicated by rapid reduction in total pressure ratio for a narrow range of intake mass flow ratio, which corresponds to

https://doi.org/10.1017/S0001924000006114 Published online by Cambridge University Press

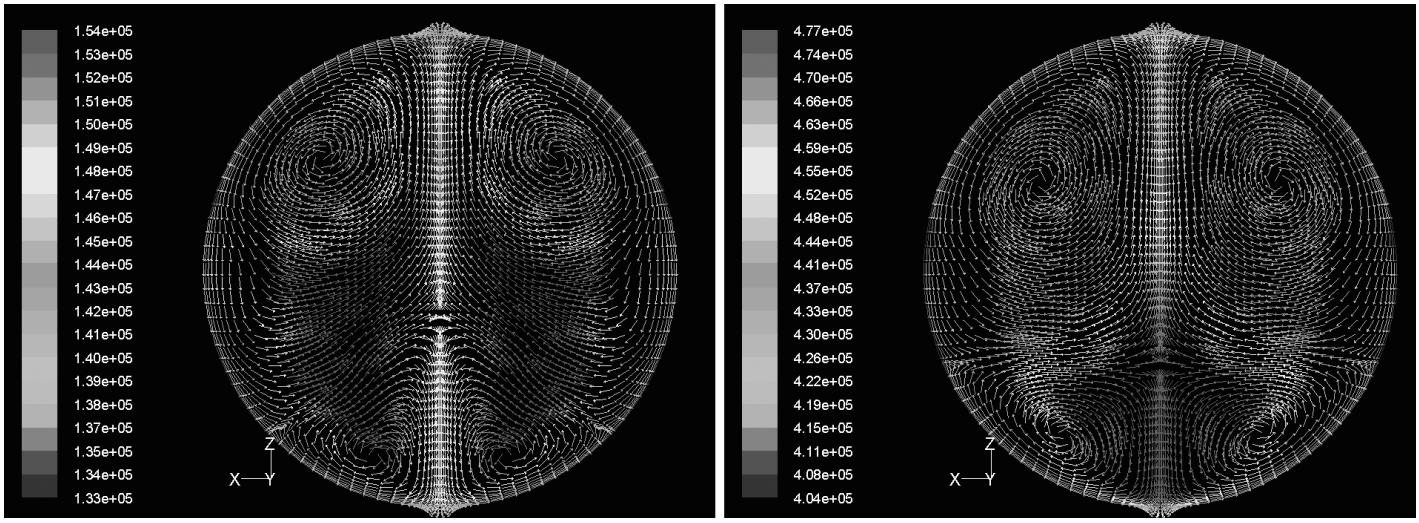

Figure 10. Secondary flow at the engine face plane at M_∞ = 0·8 (left) and M_∞ = 1·7 (right) (in-plane uniform velocity vectors coloured by total pressure (Pa)).

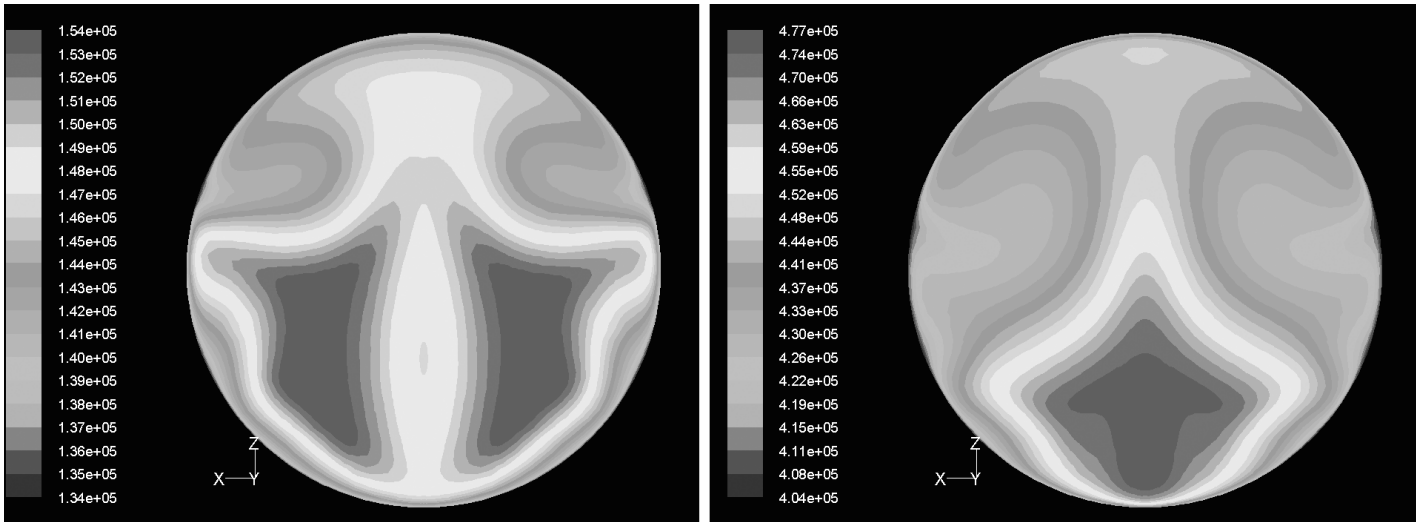

Figure 11. Total pressure (Pa) distribution at the engine face plane at M_∞ = 0·8 (left) and M_∞ = 1·7 (right).

the extreme points at highest mass flow ratio in Fig. 12. The overall qualitative subsonic pressure recovery characteristic of the present DSI (Fig. 12) is consistent with other fixed geometry inlets.

Figure 13 shows the supersonic intake total pressure recovery (ratio) at M = 1·7 at AOA = 0° and β = 0°, for a range of intake mass flow ratios. At high supersonic speeds, the total pressure recovery characteristics at engine face plane is dependent on the intake duct flow but also, to a greater extent, on the intake inlet shock wave structure. The conventional supersonic behaviour for a external compression fixed intake is that as the mass flow ratio increases from a sub-critical level, the total pressure ratio (recovery) also increases due to inlet shock waves adopting a structure progressively closer to the design point structure[19,24] (Fig. 7). Beyond the design point mass flow ratio (intake super critical operation), the inlet shock waves are generally ingested into the intake duct with rapidly deteriorating total pressure recovery. This behaviour is shown as the 'Conventional trend' line in Fig. 13.

The present DSI pressure recovery characteristics is better than the conventional trend for low-to-moderate mass flow ratios (Fig. 13). This is due to oblique/normal shock wave structure, at low mass flow ratio, retaining some resemblance to design point structure (shown in Fig. 7), which is generally not seen for other fixed geometry conventional (splitter plate/wedge type) inlets. The inlet shockwave (oblique/normal) structure is shown in Fig. 14 for near design point as well as low mass flow ratio condition. The low mass flow ratio condition in Fig. 14 corresponds to the least value point in Fig. 13. As can be seen from Fig. 14, even at low mass flow ratio, the oblique shockwave is well defined and strong whereas the normal shock wave is apparently weaker and somewhat diffused towards the bump compression surface. This indicates that at low mass flow ratio, the oblique shockwave is stronger than the design point condition, whereas the normal shockwave is weaker than the design point condition. In this case the low mass flow ratio condition is expected to have comparable or better total pressure recover than design point condition, which is essentially what is indicated in Fig. 13.

The diffused normal shock wave closer to the bump compression surface at low mass flow ratio indicates low speed flow (subsonic), as seen in Fig. 14. The same low speed flow increases the 'apparent' thickness of the bump compression surface to the oncoming (upstream) supersonic flow that results in the stronger-than-design oblique shockwave, as discussed earlier. This behaviour can be seen from comparative study of Fig. 14. The cause for this low speed flow is twofold; first the stronger oblique shockwave thickens the low energy flow layer as seen in Fig. 14. Secondly, significant

https://doi.org/10.1017/S0001924000006114 Published online by Cambridge University Press

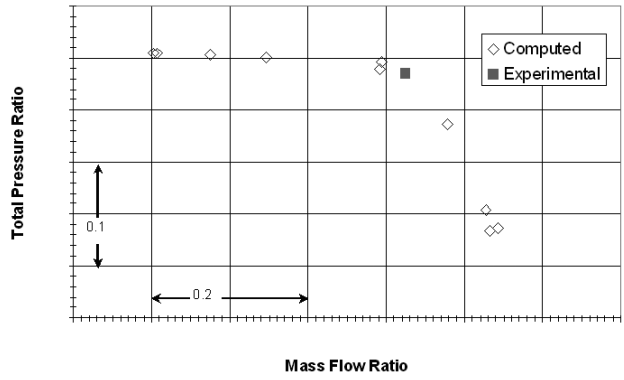

Figure 12. Total pressure recovery for various intake mass flow ratios at $M_\infty = 0{\cdot}8$, experimental data from Ref. 14.

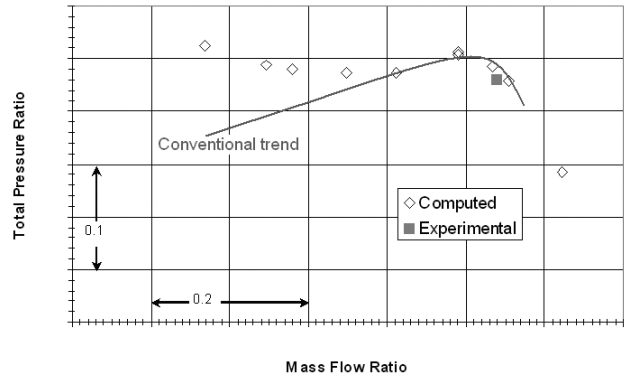

Figure 13. Total pressure recovery for various intake mass flow ratios at $M_\infty = 1{\cdot}7$, experimental data from Ref. 14.

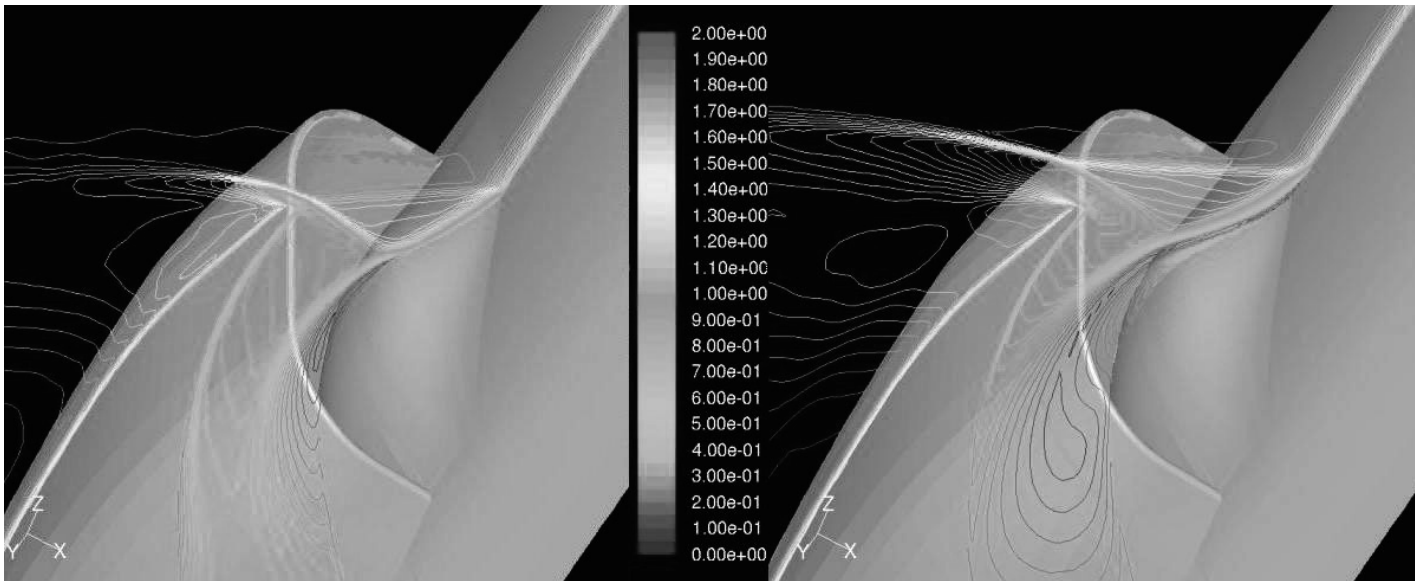

Figure 14. Mach number distribution on a horizontal plane (parallel to *x-y* plane) near design mass flow ratio (left) and low mass flow ratio (right) at $M_\infty = 1{\cdot}7$.

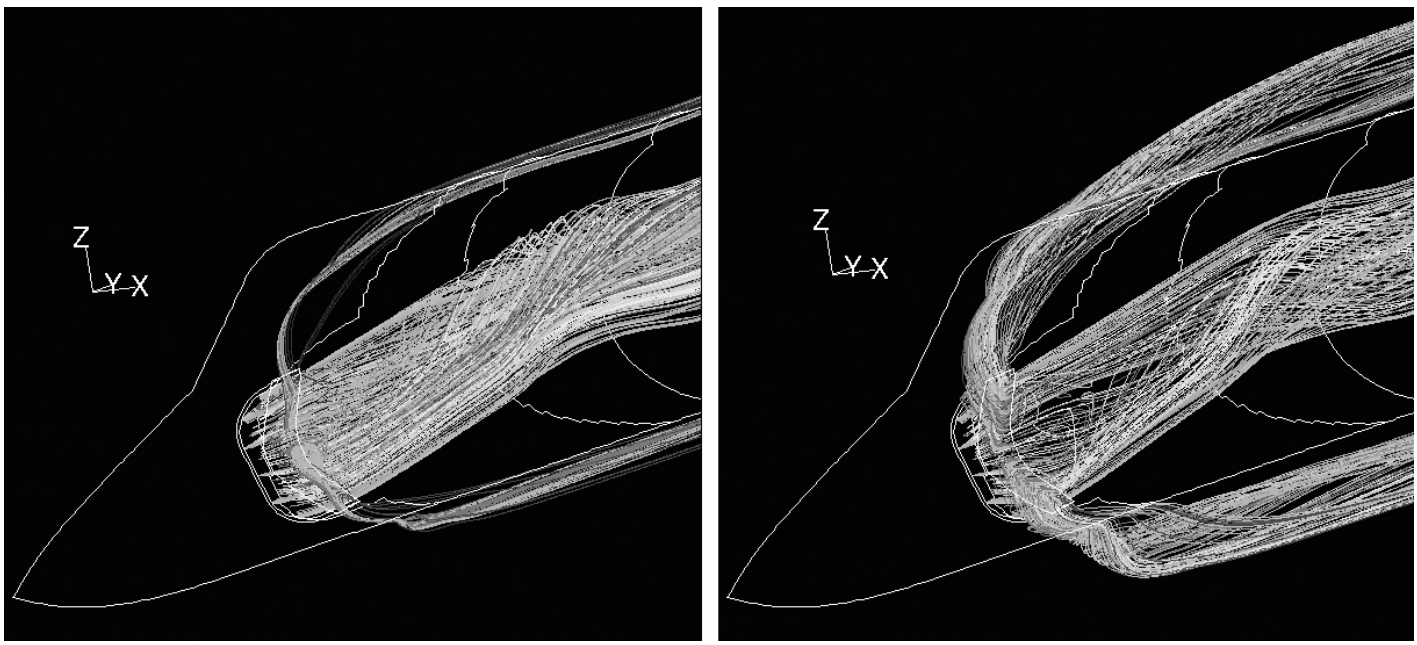

Figure 15. Stream traces from duct inlet face near design mass flow ratio (left) and low mass flow ratio (right) at $M_\infty = 1{\cdot}7$.

https://doi.org/10.1017/S0001924000006114 Published online by Cambridge University Press

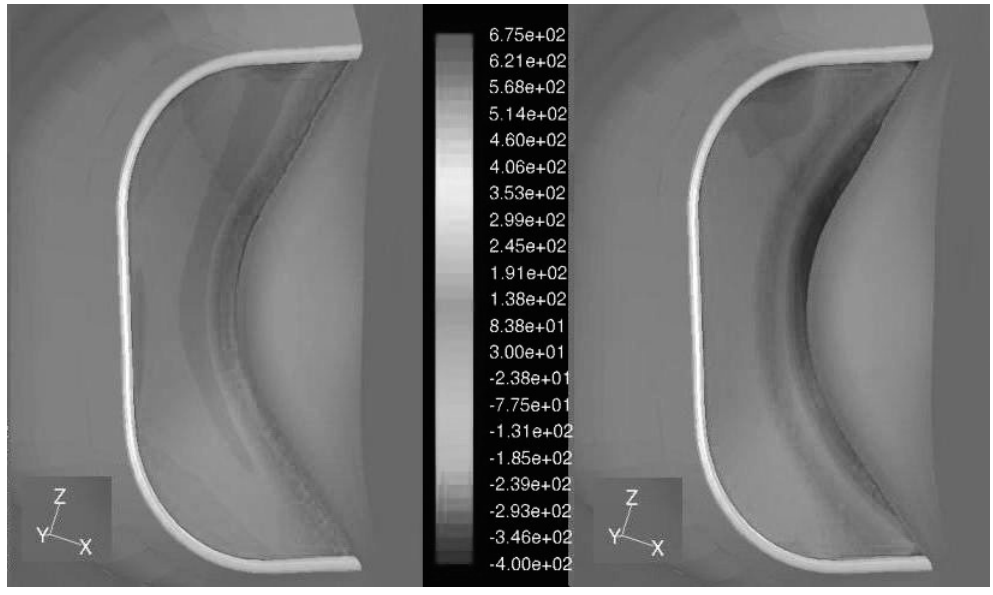

Figure 16. *Y*-velocity (ms^{-1}) contours on inlet face near design mass flow ratio (left) and low mass flow ratio (right) at M_∞ = 1·7.

amount of low energy flow is diverted outwards from the duct inlet face at low mass flow ratio compared to the near design mass flow ratio, this is shown in Fig. 15, where flow stream traces emitted by the duct inlet face are shown for near design mass flow ratio and low mass flow ratio condition consistent with Fig. 14. The region of diverted flow is restricted towards the bump compression surface, which is facilitated by the inlet cowl/lip forward sweep design. The thickened low energy/diverted flow layer is clearly shown in Fig. 16, where *y*-velocity (free stream flow direction) component is plotted on the inlet face. As can be seen from this figure (Fig. 16), at low mass flow ratio, significant region near the bump compression surface has diverted flow (negative *y*-velocity) and low energy (low *y*-velocity). This diverted flow phenomenon at low mass flow ratio, in the vicinity of the bump compression surface, causes stronger oblique and weaker normal shockwave with higher-than-conventional total pressure recovery, as indicated in Fig. 13. However, the high volume of diverted flow at sub-critical conditions (Fig. 15) causes strong interactions with external supersonic flow, which causes severe aircraft drag rise.

The higher-than-conventional pressure recovery at less-than-design mass flow ratio (sub-critical conditions) at supersonic speeds (Fig. 13) eliminates the need for an extensive air bleed system to manage the inlet shock wave structure at sub-critical conditions[14,19]. This is one of the advantages of the present DSI over other fixed inlets[14].

CONCLUSION

In this paper the flow and performance characteristics of an in-service integrated DSI are computed at zero angle-of-attack. The operating mechanism of DSI in getting rid of the upstream boundary layer at subsonic and supersonic conditions has been demonstrated and its basic pressure recovery characteristics have been quantified for both subsonic and supersonic flight conditions, which are in general agreement with wind tunnel test results at design point mass flow rates. The integrated DSI shows higher-than-conventional computed pressure recovery characteristics at sub-critical operation (low mass flow rates), which is attributed to DSI overall design that results in modified inlet shockwave structure with diverted flow concentrated near the DSI bump surface.

ACKNOWLEDGMENT

The author gratefully acknowledges the use of Computer Aided Engineering Lab (CAEL) of the Institute of Avionics and Aeronautics, Air University, Islamabad, Pakistan.

REFERENCES

1. SIMON, P.C., BROWN, D.W. and HUFF, R.G. Performance of external-compression bump inlet at Mach numbers of 1·5 and 2·0, 1957, NACA Report NACA-RM-E56L19.
2. SÓBESTER, A. Tradeoffs in jet inlet design: A historical perspective, *J Aircr*, 2007, **44**, (3), pp 705-717.
3. LI, B. and LIANG, D. Numerical simulation and experiment of integral flow field of diverterless supersonic inlet/forebody, *Hangkong Xuebao/Acta Aeronautica et Astronautica Sinica*, 2009, **30**, (9), pp 1597-1604.
4. KIM, S.D. Aerodynamic design of a supersonic inlet with a parametric bump, *J Aircr*, 2009, **46**, (1), pp 198-202.
5. LIM, S., KOH, D.H., KIM, S.D. and SONG, D.J. A computational study on the efficiency of boundary layer bleeding for the supersonic bump type inlet, 2009, AIAA-2009-34, 47th AIAA Aerospace Sciences Meeting, 5-8 January 2009, Orlando, Florida, USA.
6. XIE, W. and GUO, R. Flow field of ventral diverterless high offset *s*-shaped inlet at transonic speeds, *Hangkong Xuebao/Acta Aeronautica et Astronautica Sinica*, 2008, **29**, (6), pp 1453-1459.
7. XIE, W. and GUO, R. A ventral diverterless high offset s-shaped inlet at transonic speeds, *Chinese J of Aeronautics*, 2008, **21**, (3), pp 207-214.
8. YANG, Y.-K. Research of bump inlet design and test, *Kongqi Donglixue Xuebao/Acta Aerodynamica Sinica*, 2007, **25**, (3), pp 336-338.
9. ZHONG, Y.-C., YU, S.-Z. and WU, Q. Research of bump inlet (DSI) model design and its aerodynamic properties, *Hangkong Dongli Xuebao/J of Aerospace Power*, 2005, **20**, (5), pp 740-745.
10. TILLOTSON, B., LOTH, E., DUTTON, J., MACE, J. and HAEFFELE, B. Experimental study of a Mach 3 bump-compression flowfield, *J Propulsion and Power*, 2009, **25**, (3), pp 545-554.
11. WOODEN, P. Use of CFD in developing the JSF F-35 outer mold lines, 2006, AIAA-2006-3663, 24th AIAA Applied Aerodynamics Conference, 5-8 June 2006, San Francisco, CA, USA.
12. HEWSON, R. Sino-Pakistani fighter improved, *Jane's Defence Weekly*, December 2005, pp 99-100.
13. JENNINGS, G. JF-17 Production Commences, *Jane's Defense Weekly*, 24 January 2008.
14. YANG, Y. Design of bump inlet of Thunder/JF-17 aircraft, *J of Nanjing University of Aeronautics & Astronautics*, August 2007, **39**, (4), pp 449-452.

https://doi.org/10.1017/S0001924000006114 Published online by Cambridge University Press

15. GAMBIT, Geometry and Mesh Generation Software Package, Ver. 2.2.30, Fluent Inc, Lebanon, NH, USA.
16. FLUENT, Computational Fluid Dynamics Software Package, Ver. 6.3.26, Fluent Inc, Lebanon, NH, USA.
17. FLUENT, Computational Fluid Dynamics Software Package User Guide, Version 6.3, Fluent Inc, Lebanon, NH, USA.
18. SPALARAT, P. and ALLMARAS, S. A one-equation turbulence model for aerodynamic flows, 1992, Technical Report AIAA-92-0439, American Institute of Aeronautics and Astronautics.
19. SEDDON, J. and GOLDSMITH, L. *Intake Aerodynamics*, 1999, London: Blackwell Science .
20. TAN, H.-J. and GUO, R.-W. Numerical simulation investigation and experimental validation of a top-mounted diverterless inlet and its validation, *Hangkong Xuebao/Acta Aeronautica et Astronautica Sinica*, 2004, **25**, (6), pp 540-545.
21. TAN, H.-J. and GUO, R.-W. Design and wind tunnel study of a top-mounted diverterless inlet, *Chinese J Aeronautics*, 2004, **17**, (2), pp 72-78.
22. LIANG, D.-W. and LI, B. Inverse design of diverterless inlet and mechanism of diversion of boundary layer, *Hangkong Xuebao/Acta Aeronautica et Astronautica Sinica*, 2005, **26**, (3), pp 286-289.
23. KIM, S.D., SONG, D. J. and LIM, SL. Numerical analysis on three-dimensional flow field in a supersonic bump inlet, 2007, AIAA-2007-689, 45th AIAA Aerospace Sciences Meeting and Exhibit, 8-11 January 2007, Reno, NV, USA.
24. OATES, G.C. (ED). Aircraft Propulsion System Technology and Design, 1989, AIAA Education Series, published by the American Institute of Aeronautics and Astronautics.
25. HAMSTRA, J.W., MCCALLUM, B.N., SYLVESTER, T.G., DENNER, W. and MOOREHOUSE, J.A. Transition shoulder system and method for diverting boundary layer air, 1998, United States Patent 5749542.
26. HAMSTRA, J.W. and SYLVESTER, T.G. System and method for diverting boundary layer air, 1997, International application published under the Patent Cooperation Treaty WO 97/35105.

https://doi.org/10.1017/S0001924000006114 Published online by Cambridge University Press